



A New Field Line Tracer for the Study of Coronal Magnetic Topologies

Valentin Aslanyan¹ , Roger B. Scott² , Chloe P. Wilkins³ , Karen A. Meyer¹ , David I. Pontin³ , and Anthony R. Yeates⁴ ¹Division of Mathematics, School of Science and Engineering, University of Dundee, Dundee, DD1 4HN, UK; vaslanyan001@dundee.ac.uk²US Naval Research Laboratory, Washington, DC 20375, USA³School of Information and Physical Sciences, University of Newcastle, University Drive, Callaghan, NSW 2308, Australia⁴Department of Mathematical Sciences, Durham University, Durham, DH1 3LE, UK

Received 2024 April 16; revised 2024 June 6; accepted 2024 June 6; published 2024 August 13

Abstract

We present a new code for the tracing of magnetic field lines and calculation of related quantities such as the squashing factor in the solar corona. The Universal Fieldline Tracer (UFiT) is an open-source package that can currently take inputs directly from four well-established coronal models, with additional models planned to be made directly accessible in the future. This package contains tools to make use of large-scale three-dimensional field line maps to calculate volumetric quantities, such as the total volume of the open corona, or the fraction that maps to regions on the solar surface within some distance of a coronal hole boundary, which may be relevant to phenomenological models of solar wind speed such as the Wang–Sheeley–Arge model. Synthetic coronagraphs can also be produced rapidly by this package. We have postprocessed long-term magnetofrictional simulations to demonstrate that the separatrix web occupies a larger fraction of the corona during solar maximum than solar minimum.

Unified Astronomy Thesaurus concepts: [Solar corona \(1483\)](#); [Computational methods \(1965\)](#); [Open source software \(1866\)](#)

Materials only available in the [online version of record](#): [animation](#)

1. Introduction

The topology of the magnetic field of the solar corona has been a topic of intense research in recent times. Accurate determination of field structure can yield insights into the processes of magnetic reconnection, solar wind formation, and generation of various solar ejecta. Adjacent field lines frequently diverge—with mappings which are often discontinuous—forming the separatrix web (S-Web; Antiochos, et al. 2011) throughout the solar corona. Such locations of rapid field-line divergence are well established as preferential locations for the formation of current sheets and subsequent reconnection, driving various dynamic phenomena (e.g., Pontin & Priest 2022). Thus, an important mathematical quantity for the analysis of magnetic reconnection is the squashing factor Q (Titov et al. 2002), which takes large values where magnetic field lines are divergent or helical.

In this article, we present a new code—Universal Fieldline Tracer (UFiT)—which can rapidly calculate field line connectivities, squashing factors, and flux surfaces. This code is an attempt to standardize these types of calculations, taking inputs directly from common approaches such as potential field source surface (PFSS) models, magnetohydrodynamic and magnetofrictional solvers, and returning the same structure of output in all cases. This greatly simplifies comparisons between the different models, improves portability, and streamlines further postprocessing tools relying on field line trajectories.

UFiT is intended to be universal in the sense that it can read the magnetic field directly from the outputs of a number of popular codes. It does so using minimalist in-built routines, without requiring specialist libraries or even the original code

used to calculate the magnetic field. The field lines shown in Figure 1 have been computed from the following sources, with geometry indicated: (a) Durham Magnetofrictional Code (DUMFRIC; see Yeates & Bhowmik 2022); (b) Lare3d; Adaptively Refined Magnetohydrodynamic Solver (ARMS; see DeVore 1991) with (c) spherical and (d) Cartesian coordinates; (e) the `pfsspy` package (see Stansby et al. 2020) taking as input a synoptic magnetogram derived from observations by the Helioseismic and Magnetic Imager (HMI) instrument on board the Solar Dynamics Observatory (Pesnell et al. 2012); and (f) an analytic formula evaluated on a grid of points in Python. The squashing factor Q is also shown on a surface of constant r and z , respectively. In the first five cases, UFiT identified the type of output from the file name (for example, Lare3d outputs have the `.sdf` extension) and then read in the grid and the magnetic field defined on it; in the latter case, UFiT had a grid and field passed to it programmatically.

UFiT is written in Fortran90 requiring only the OpenMP library to be installed for normal operation. This leads to an almost linear scaling with processor number. The total real time taken to compute a 1000×1000 grid of field lines is of the order of a minute, utilizing the cores of a modern laptop computer. The DUMFRIC code outputs data in the NetCDF format which requires that particular library to be installed, but UFiT can be compiled without it and still use the remaining sources in Figure 1. The initial UFiT 1.0 release is available from Zenodo at doi:10.5281/zenodo.10301324 (Aslanyan & Meyer 2023), while the latest version is available from GitHub (Aslanyan 2024).⁵

In this article, we define the mathematical approach to compute the field lines and, in particular, the squashing factor in Cartesian and spherical coordinates. We validate UFiT against an analytical solution and other field line tracing codes. We then visualize the structure of an eruption and the

Original content from this work may be used under the terms of the [Creative Commons Attribution 4.0 licence](#). Any further distribution of this work must maintain attribution to the author(s) and the title of the work, journal citation and DOI.

⁵ <https://github.com/Valentin-Aslanyan/UFiT>

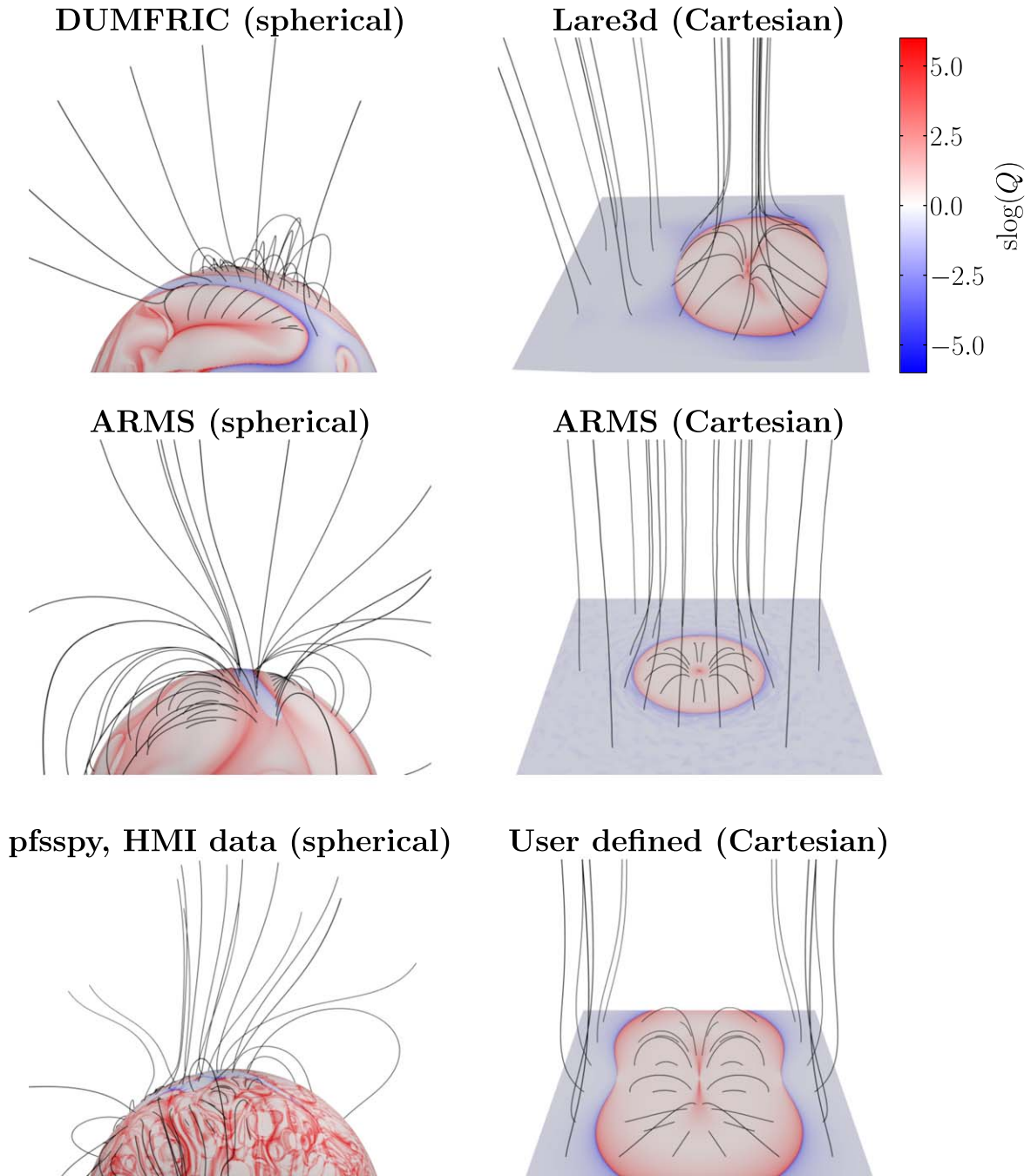


Figure 1. The signed logarithm of the squashing factor, $\text{slog}(Q) \equiv \pm \log(Q)$ where the + denotes closed field lines and the - all others, on an appropriate surface (constant r for spherical geometries and constant z for Cartesian). Sample open and closed magnetic field lines are shown. UFiT has been used to read in the magnetic field from outputs of codes indicated.

subsequent open field, as relevant to the expulsion of solar wind, using tools published with UFiT. We proceed to use UFiT to analyze a dynamically evolving coronal magnetic field using a further postprocessing library.

2. Field Line and Squashing Factor Calculation

UFiT calculates magnetic field lines in both directions from a set of start or “seed” points, which are specified by the user either as a regular one-, two-, or three-dimensional grid or point by point. Based on the user configuration, UFiT saves any combination of the locations where the field lines terminate, the full field line trajectories, the perpendicular magnetic squashing

factor Q (sometimes called Q_{\perp}) of the field line, the type of connectivity (see Table 1). Alternatively, a user-defined quantity is calculated by an existing subroutine template and saved; thus, the user can rapidly implement a subroutine to calculate a desired quantity such as $\max(|\mathbf{B}|)$ along a field line. The start configuration is also saved within the output file.

The first step to calculate magnetic field lines from a variety of sources is to convert the input grid to a set of consistent coordinates. Presently implemented in UFiT are Cartesian (x, y, z) and spherical (r, θ, ϕ) coordinate systems, related in the usual way,

$$x = r \sin \theta \cos \phi, \quad (1)$$

Table 1
Terms Related to Magnetic Field Line Topology Defined for the Purposes of This Article

Term	Definition
Footpoint	Location where a given field line crosses the solar photosphere (or similar surface), which is represented as the lowest grid value, z_{\min} or r_{\min} , respectively
Handhold	Location where a given field line crosses the highest grid value, z_{\max} or r_{\max} , respectively
Closed	Field line with exactly two footpoints
Open	Field line with exactly one footpoint and one handhold
Disconnected	Field line with exactly two handholds

$$y = r \sin \theta \sin \phi, \quad (2)$$

$$z = r \cos \theta, \quad (3)$$

where the polar angle θ and azimuthal angle ϕ take the usual ranges of values

$$\theta \in [0, \pi), \quad (4)$$

$$\phi \in [0, 2\pi), \quad (5)$$

with $\theta = 0$ the north pole. The initial seed points of the field lines are supplied to `UFiT` and outputs are returned in one of the above sets of coordinates, in addition to a flag for the corresponding coordinate system. The `Python` interface to the code allows easy translation to and from other coordinate systems as required.

The magnetic field \mathbf{B} is evaluated at arbitrary points within the simulation domain by linear interpolation from the nearest eight grid points, in the relevant coordinate system. When required, the gradient is calculated by differentiating the interpolation formula directly. See Appendix A for more details.

2.1. Field Lines

The equation for the position $\mathbf{X}(l)$ along a field line, parameterized by the distance l along the field line, is given by

$$\frac{d\mathbf{X}}{dl} \equiv \left(\frac{\mathbf{B}}{|\mathbf{B}|} \cdot \nabla \right) \mathbf{X} = \frac{\mathbf{B}}{|\mathbf{B}|}. \quad (6)$$

Rewriting this term explicitly for a given system of coordinates requires the correct coordinate scale factors. These are unity for Cartesian, leading to the familiar relations,

$$\frac{dx}{dl} = \frac{B_x}{|\mathbf{B}|}, \quad (7)$$

$$\frac{dy}{dl} = \frac{B_y}{|\mathbf{B}|}, \quad (8)$$

$$\frac{dz}{dl} = \frac{B_z}{|\mathbf{B}|}. \quad (9)$$

In spherical coordinates the scale factors are taken from the diagonal entries of the metric (see Appendix B). The

appropriate equations are given by

$$\frac{dr}{dl} = \frac{B_r}{|\mathbf{B}|}, \quad (10)$$

$$\frac{d\theta}{dl} = \frac{1}{r} \frac{B_\theta}{|\mathbf{B}|}, \quad (11)$$

$$\frac{d\phi}{dl} = \frac{1}{r \sin \theta} \frac{B_\phi}{|\mathbf{B}|}. \quad (12)$$

These systems of equations are solved by iterative integration methods. We plan on including higher-order, adaptive methods, but surprisingly find that the first-order Euler method performs very reasonably (see Section 3). This choice of integrator proves beneficial, both in terms of calculating the boundary intercept (see below), and as a comparison to other codes that also use Euler steps (such as `QSLsquasher` and the visualization routine for `ARMS`). A fixed size of the integration step Δl , which in `UFiT` may be specified by the user, is advantageous in postprocessing and storing the resultant field lines. `UFiT` defaults to a step size of $\Delta l = 0.005 R_\odot$, which was found to provide good accuracy for a typical field configuration while keeping the computation times low.

Each seed point serves as an initial value for the field line equation, corresponding to a position of $\mathbf{X}(l=0)$ along the field line. The integration proceeds in each of two directions from the initial seed location until a domain boundary is intercepted or a preset total number of steps is reached. In terms of the position along the field line, the location of the forward and backward domain boundaries are given by l_+ and l_- , and the points at which the field line intersects these boundaries are $\mathbf{X}(l_+)$ and $\mathbf{X}(l_-)$. In some special cases, such as in the presence of current loops, in laboratory experiments or simulations with artificial symmetry (see Yeates & Hornig 2016), magnetic field lines may close on themselves within a typical simulation volume, or they may traverse a subvolume ergodically. Almost always, however, a field line will terminate at one or two of the boundaries of the simulation domain. We define several terms in Table 1 related to the termination of field lines. These are determined directly by inspection of the field line end points $\mathbf{X}(l_+)$ and $\mathbf{X}(l_-)$. The labels are assigned at the seed points, meaning that they represent volumetric data that is inherited from the field lines that pass through each point in the volume.

At each integration step, a check is made whether the step will intercept any of the boundaries. If so, a shortened step is taken, the integration terminates, and the appropriate connectivity is assigned. This check is skipped if a given axis is specified to have periodic boundary conditions, in which case the integration proceeds forward and the coordinate is allowed to exceed the limits. Suppose that one of the coordinates above, $c \in \{x, y, z, \theta, \phi\}$ is defined as periodic; for the purposes of interpolation, the position of coordinate c is remapped to within the original grid limits through the relation

$$c' = [(c - c_{\min}) \bmod (c_{\max} - c_{\min})] + c_{\min}. \quad (13)$$

For example, suppose that a field line is spiraling out from the Sun in a spherical simulation domain with periodicity in longitude. The angle ϕ in the output of `UFiT` will grow monotonically, quickly exceeding 2π , but internally, it will at every step be remapped to the range $[0, 2\pi)$. The polar angle θ

is a special case. For many spherical simulation domains, it is truly nonperiodic, with the grid taking the form of a wedge by design; a field line may terminate on a boundary in θ . Other simulations deliberately encompass the entire range of polar angles, in which case a field line θ may go below 0 (crossing over the north pole), or above π (over the south pole). If this happens in a fully spherical domain, θ is restored back to the correct range while ϕ is incremented or decremented by π as required.

2.2. Squashing Factor

As introduced and then developed in a series of papers, the squashing factor (Q) is a measure of the deformation of the field line mapping that is calculated using elements of the Jacobian of the mapping (Priest & Démoulin 1995; Titov et al. 2002; Titov 2007). Early computational implementations took the approach of calculating the field line mapping (typically by integrating a large number of field lines), and then evaluating derivatives of this mapping using finite differences, before finally performing appropriate multiplications between these derivative terms. For complex magnetic fields in particular, the squashing factor distribution thus constructed is susceptible to noise, which motivated Pariat & Démoulin (2012) to explore various different protocols for the field line integrations. However, as first suggested by Tassev & Savcheva (2017) and then formalized by Scott et al. (2017), it turns out that Q can also be calculated by propagating vectors that directly encode the information about the mapping Jacobian, avoiding the need for finite differences. This formalism has now been implemented in a number of freely available codes (Zhang et al. 2022; Yang 2024), typically requiring significantly shorter computation times for equivalent quality data outputs.

The method for calculating Q in `UFiT` is taken from the formalism described in Scott et al. (2017), and is similar in many ways to the methods of Tassev & Savcheva (2017), Zhang et al. (2022), and Yang (2024). When selected by the user, Q is calculated alongside the usual field line tracing in the Cartesian or spherical geometry using the following procedure. For each seed point we initialize a pair of unit vectors, \mathbf{U} and \mathbf{V} , which are mutually orthonormal and perpendicular to \mathbf{B} . The vectors \mathbf{U} and \mathbf{V} are then transported along $\mathbf{X}(l)$ according to the Lie transport equation, which, in the case of \mathbf{U} , takes the form

$$\frac{d\mathbf{U}}{dl} = \left(\frac{\mathbf{U}}{|\mathbf{B}|} \cdot \nabla \right) \mathbf{B}, \quad (14)$$

and similarly for \mathbf{V} .

In Cartesian coordinates the component form of this system of equations is written (using \mathbf{U} as an example) as

$$\frac{dU_x}{dl} = \frac{1}{|\mathbf{B}|} \left(U_x \frac{\partial}{\partial x} + U_y \frac{\partial}{\partial y} + U_z \frac{\partial}{\partial z} \right) B_x, \quad (15)$$

$$\frac{dU_y}{dl} = \frac{1}{|\mathbf{B}|} \left(U_x \frac{\partial}{\partial x} + U_y \frac{\partial}{\partial y} + U_z \frac{\partial}{\partial z} \right) B_y, \quad (16)$$

$$\frac{dU_z}{dl} = \frac{1}{|\mathbf{B}|} \left(U_x \frac{\partial}{\partial x} + U_y \frac{\partial}{\partial y} + U_z \frac{\partial}{\partial z} \right) B_z. \quad (17)$$

In spherical coordinates the system of equations is similar, but with a number of extra terms related to the curvature of the

coordinate system and the coordinate scale factors, so that

$$\frac{dU_r}{dl} = \frac{1}{|\mathbf{B}|} \left(U_r \frac{\partial}{\partial r} + \frac{1}{r} U_\theta \frac{\partial}{\partial \theta} + \frac{1}{r \sin \theta} U_\phi \frac{\partial}{\partial \phi} \right) B_r, \quad (18)$$

$$\begin{aligned} \frac{dU_\theta}{dl} &= \frac{1}{|\mathbf{B}|} \left(U_r \frac{\partial}{\partial r} + \frac{1}{r} U_\theta \frac{\partial}{\partial \theta} + \frac{1}{r \sin \theta} U_\phi \frac{\partial}{\partial \phi} \right) B_\theta \\ &+ \frac{1}{|\mathbf{B}|} \frac{1}{r} (B_r U_\theta - U_r B_\theta), \end{aligned} \quad (19)$$

$$\begin{aligned} \frac{dU_\phi}{dl} &= \frac{1}{|\mathbf{B}|} \left(U_r \frac{\partial}{\partial r} + \frac{1}{r} U_\theta \frac{\partial}{\partial \theta} + \frac{1}{r \sin \theta} U_\phi \frac{\partial}{\partial \phi} \right) B_\phi \\ &+ \frac{1}{|\mathbf{B}|} \frac{1}{r} (B_r U_\phi - U_r B_\phi) \\ &+ \frac{1}{|\mathbf{B}|} \frac{\cos \theta}{r \sin \theta} (B_\theta U_\phi - U_\theta B_\phi). \end{aligned} \quad (20)$$

These expressions are derived in more detail in Appendix B.

The vectors $\mathbf{U}(l)$ and $\mathbf{V}(l)$ are transported along the field line $\mathbf{X}(l)$ using the appropriate system of equations until the field line intersects the boundary at $\mathbf{X}(l_+)$ and $\mathbf{X}(l_-)$. In order to characterize the local variation in the mapping perpendicular to the magnetic field, the components of \mathbf{U} and \mathbf{V} that are parallel to \mathbf{B} are then removed so that $\mathbf{U}(l_+)$ is perpendicular to $\mathbf{B}(\mathbf{X}(l_+))$, and similarly for the other terms. This procedure defines the appropriate tangent elements

$$\mathbf{U}_+ = \mathbf{U}(l_+) - \hat{\mathbf{B}}_+(\hat{\mathbf{B}}_+ \cdot \mathbf{U}(l_+)), \quad (21)$$

$$\mathbf{V}_+ = \mathbf{V}(l_+) - \hat{\mathbf{B}}_+(\hat{\mathbf{B}}_+ \cdot \mathbf{V}(l_+)), \quad (22)$$

$$\mathbf{U}_- = \mathbf{U}(l_-) - \hat{\mathbf{B}}_-(\hat{\mathbf{B}}_- \cdot \mathbf{U}(l_-)), \quad (23)$$

$$\mathbf{V}_- = \mathbf{V}(l_-) - \hat{\mathbf{B}}_-(\hat{\mathbf{B}}_- \cdot \mathbf{V}(l_-)), \quad (24)$$

where $\hat{\mathbf{B}}_+$ is the magnetic unit vector at the point $\mathbf{X}(l_+)$, and similarly for $\hat{\mathbf{B}}_-$.

The tangent elements have the property that, in addition to obeying the Lie transport equation, they also transform under the push-forward, which is directly related to the Jacobian (\mathbf{J}) of the field line mapping. In particular, the (square of the) norm (N) of the Jacobian can be recovered directly from \mathbf{U} and \mathbf{V} as

$$N^2 = \mathbf{U}_+^2 \mathbf{V}_-^2 + \mathbf{U}_-^2 \mathbf{V}_+^2 - 2(\mathbf{U}_+ \cdot \mathbf{V}_+)(\mathbf{U}_- \cdot \mathbf{V}_-). \quad (25)$$

Similarly, the determinant of the Jacobian is given by

$$\begin{aligned} \det(\mathbf{J}) &= \sqrt{\mathbf{U}_-^2 \mathbf{V}_-^2 - (\mathbf{U}_- \cdot \mathbf{V}_-)^2} \\ &\times \sqrt{\mathbf{U}_+^2 \mathbf{V}_+^2 - (\mathbf{U}_+ \cdot \mathbf{V}_+)^2}. \end{aligned} \quad (26)$$

Alternately, (and in the current implementation) $\det(\mathbf{J})$ can be determined from the (divergence-free) magnetic field, in which case

$$\det(\mathbf{J}) = \frac{|\mathbf{B}_0|^2}{|\mathbf{B}_+||\mathbf{B}_-|}. \quad (27)$$

The (perpendicular) squashing factor is then given by

$$Q = \frac{N^2}{\det(\mathbf{J})}. \quad (28)$$

Like the connectivity labels, the calculated value of Q is assigned to the seed point. In principle, Q is not a volumetric quantity per se, as it describes the field line mapping, which is,

itself, an integrated (global) measure. By assigning the value of Q as volumetric data, we associate the complexity of the mapping at the end points of the field lines with the seed points through which the field lines pass, with the understanding that this value describes the entire field line, and not just the seed point. Finally, we adopt the sign convention that Q (whose formal lower bound is 2) is positive for closed field lines and negative otherwise.

3. Validation

To confirm the numerical accuracy of UFiT, we have compared its results to an analytic case. We have also made a comparison with two other field line tracing codes: QSLsquasher, which has been widely used to study the corona (see Tassev & Savcheva 2017 for further details and the source code) and K-QSL (see Yang 2024 for the source code). Figure 2 shows the structure of a potential source surface field, which is purely dipolar at the photosphere. The field, and consequently the squashing factor, is axially symmetric with a central belt of closed field lines around the equator. The squashing factor at the photosphere ($r = R_\odot$) in the open field region (see Appendix C for more details) is given by

$$Q = \left\{ 1 + \frac{\cos^2 \theta}{1 - C^2 \sin^2 \theta} \left[1 + \left(\frac{R_{ss}^3 - R_\odot^3}{R_\odot^3 + 2R_{ss}^3} \right)^2 \tan^2 \theta \right] \right\} \times \sqrt{\frac{1 - C^2 \sin^2 \theta}{\cos^2 \theta + \left(\frac{R_{ss}^3 - R_\odot^3}{R_\odot^3 + 2R_{ss}^3} \right)^2 \sin^2 \theta}}, \quad (29)$$

$$C = \sqrt{\frac{2R_{ss}^3 + R_\odot^3}{3R_\odot R_{ss}^2}}, \quad (30)$$

where we have chosen $R_{ss} = 2.5 R_\odot$ for this comparison; in general, UFiT assumes R_{ss} to be the largest value of r in the input grid, which can take any arbitrary value. Within the closed field region the squashing factor takes the lowest theoretical value of $Q = 2$; it is everywhere symmetric about $\theta = \pi/2$. At the photosphere, the separatrix between the open and closed regions in the northern hemisphere is located at $\theta_{QSL} = \arcsin(1/C) \simeq 0.867$ rad.

The results of UFiT agree very closely with the analytic solution as shown in Figure 2. In the closed field region close to the separatrix, the raw solution somewhat undershoots the analytic value. However, this would ordinarily not be a problem, as the value of the squashing factor is *clamped* to force its absolute value $|Q| \geq 2$. In such a case, UFiT would match the theoretical value identically in the closed field region and to better than 1% away from the separatrix. K-QSL achieves even closer agreement with the analytic result in some places, but it should be noted that it ran significantly slower than UFiT, the former taking 27 minutes in this test compared to 11 s for the latter. Small differences with the analytic solution arise because both tracers used an input magnetic field defined on a fixed grid of (40, 90) points in (r, θ) (the dipolar field is axisymmetric, so uniform in ϕ), whereas the analytic calculation can naturally rely on an exact formula. The grid is

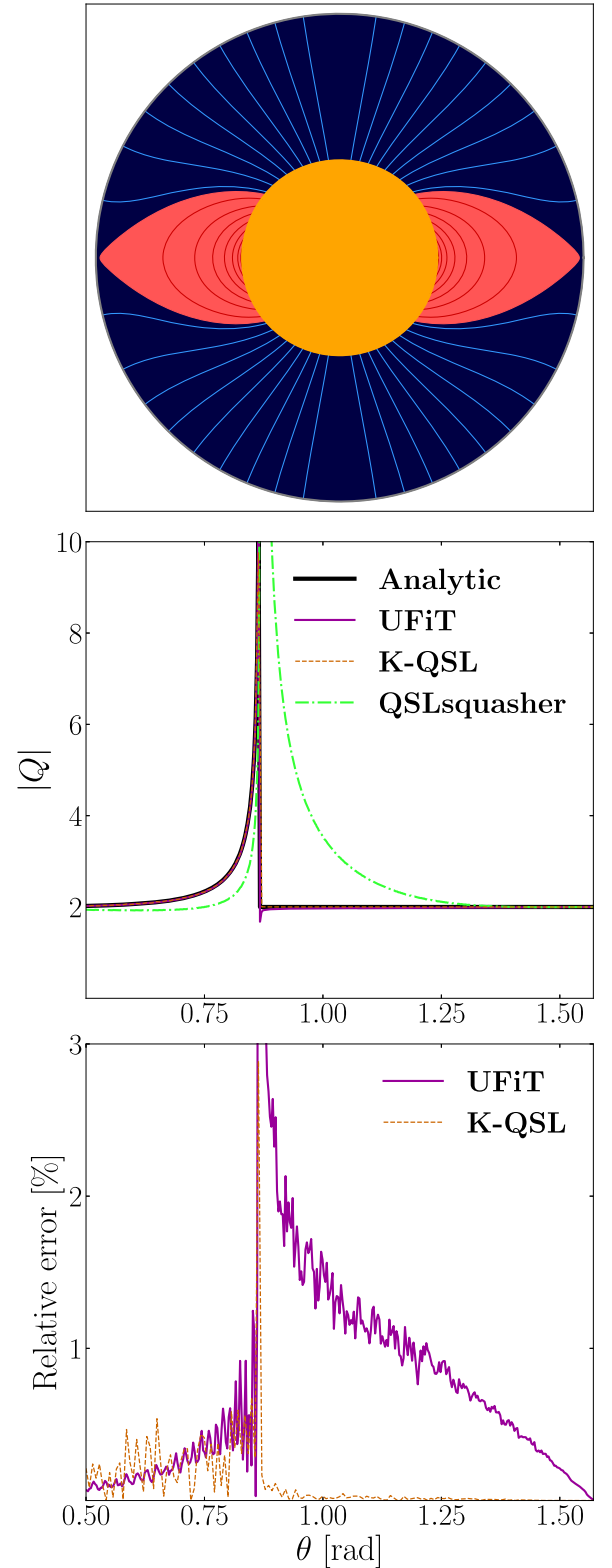


Figure 2. Open and closed field lines for a pure dipolar potential magnetic field (upper). Comparison of Q between the analytic solution and numerical results from UFiT, K-QSL, and QSLsquasher (middle). The relative error $|Q - Q_{analytic}|/Q_{analytic}$ (lower). Q is compared at $r = R_\odot$ where the separatrix occurs at $\theta \simeq 0.867$ rad and is symmetric about $\theta = \pi/2$. Note that the raw result is being shown from UFiT in the closed field region; it would ordinarily be clamped to the value of 2, thereby reproducing the analytic result exactly.

quite coarse, leading to interpolation errors, but its size is realistic for what a user may choose for a dynamic global coronal simulation. The integration step size was set at $\Delta l \simeq 0.005 R_{\odot}$. Both codes can approach the analytic values of Q to arbitrary precision if the interpolant grid resolution is increased and the integration step size is decreased. Given that UFiT has a significantly shorter computation time, the user is free to decrease the integration step size to achieve higher numerical precision.

We also make a comparison with the QSLsquasher code, which used an input magnetic field defined on a grid of (61, 181) points in (r, θ) . This code produces $Q > 2$ in the closed field region and underestimates Q in the open field region, consequently deviating significantly from the analytical result. We believe that this discrepancy arises because QSLsquasher omits the terms pertaining to curvature (the commutators in Equations (18), (19), (20)). Numerical experiments have been able to reproduce the closed field behavior by omitting the curvature terms, but in that case Q differs in the open field region from both QSLsquasher and the analytic result.

Furthermore, we have compared the squashing factors computed by UFiT and QSLsquasher for a more realistic scenario in Figure 3. The input in each case is an output from a three-dimensional spherical magnetofrictional simulation using the code DUMFRIC at 12:00 on 1992 February 4 (see Aslanyan et al. 2024 for further details of the simulation). Both field line tracing codes were supplied an identical input grid, and an identical output grid was returned. Despite its disagreement with the analytic case, the output of QSLsquasher produces large values of Q in the same locations as UFiT, highlighting the topological features, such as pseudostreamers. When compared directly, both codes produce a very similar structure, differing mostly along separatrices where Q tends to infinity. Both codes took a similar time to complete their calculations; the speedup stemming from the use of a GPU in the case of QSLsquasher was counteracted (in the experience of the authors) by the memory transfer latency.

4. Flux Surfaces and Volumetric Quantities

One concept relevant to the discussion of magnetic field topologies is that of a flux surface: a two-dimensional surface to which the magnetic field is everywhere a tangent vector. This implies that a normal vector to a flux surface is also normal to the local magnetic field, $\mathbf{n} \cdot \mathbf{B} = 0$. Since the property of being tangent to the field is also the defining principle of a field line, a flux surface is one within which magnetic field lines lie. In general, we define a flux surface as a locus of all field lines with a given property. For example, the last closed flux surface (LCFS) which separates open and closed field lines, is defined as the surface of all closed field lines which pass infinitesimally close to an open or disconnected field line. The LCFS will typically consist of a streamer belt running around the midplane of the Sun, pinned to the outer simulation boundary in typical models approaching the Parker solution. Pseudostreamers cause bulges in the LCFS, separate from the main streamer belt.

Similarly, the first disconnected flux surface (FDFS) is the locus of all disconnected field lines passing infinitesimally close to open and closed field lines. This surface arises due to magnetic reconnection in a nonpotential, nonequilibrium situation such as an eruption. It is also possible to define more general flux surfaces, for example, as the locus of all open field

lines with a specified shortest distance from a footpoint to a coronal hole boundary, d_{CHB} . The coronal hole boundary is on the photosphere, and the distance between two points here is taken to be Euclidean in Cartesian coordinates,

$$d = \sqrt{(x_1 - x_2)^2 + (y_1 - y_2)^2} \quad (31)$$

and the great circle distance in spherical coordinates,

$$d = \arccos(\cos \theta_1 \cos \theta_2 + \sin \theta_1 \sin \theta_2 \cos(\phi_1 - \phi_2)). \quad (32)$$

We adopt the same sign convention for d_{CHB} as for Q , namely that closed field lines correspond to a positive value and all others to a negative value. A flux surface defined by d_{CHB} is physically meaningful because it has long been observed that a portion of the slow solar wind emerges from near coronal hole boundaries due to the interchange reconnection between open and closed field lines Abbo et al. (2016), while the fast wind is accelerated from the central regions of coronal holes. In the latest version of the Wang–Sheeley–Arge (WSA) model (Wang & Sheeley 1990; Arge et al. 2003), for example, the solar wind speed on open field lines is a function of d_{CHB} (see Kim et al. 2020 for recently used parameters).

We show examples of these three types of flux surface (each at a different time), for a magnetic field computed by the DUMFRIC code (see Aslanyan et al. 2024 for further details of the simulation). In brief, the magnetofrictional code DUMFRIC was initialized with a PFSS reconstruction on 1975 September 25 from KPVT synoptic magnetogram CR 1633 and thereafter self-consistently computed the evolving magnetic until 2022 November 25; the output magnetic field was saved at a frequency of once per week, or more. Solar activity was modeled by enforcing the emergence of active regions, taken directly from observations determined from KPVT, SOLIS, and HMI synoptic magnetograms, and thereafter applying differential rotation, meridional flows, and surface diffusion to approximate the effect of flux dispersal due to supergranulation (see Yeates & Bhowmik 2022). The code modeled the emergence of Active Region 12672 around 2017 August 25, which caused an eruption and associated change in magnetic connectivity. The LCFS is shown 24 hr after the emergence of the active region in Figure 4(a), with a full view around the simulation domain available in the animated version of this figure. A highly twisted and knotted surface can be seen. The eruption has caused field lines to become disconnected and hence the FDFS is shown 42 hr after the emergence of the active region in Figure 4(b). It is noteworthy that this surface has several holes, indicating that open field lines are threaded through the bulk of the disconnected ejecta. Finally, the field lines relax toward a new dynamic equilibrium; a flux surface 96 hr after the emergence of the active region is shown in Figure 4(c). This flux surface corresponds to $d_{\text{CHB}} = -15$ Mm and consequently it can be expected that fast wind is flowing out through the volume outside this surface. The super-radial expansion of the magnetic field can be seen from the trumpet-like openings of this flux surface. The flux surface is more corrugated, and some narrow features appear broken up, due to the greater topological complexity of this type of flux surface.

The LCFS is generated by first computing a binary three-dimensional grid such that the seed points of closed field lines take the value 0, and 1 otherwise. A Gaussian filter is applied to smooth out the resultant structure. A marching cubes algorithm is applied to the resultant grid with a threshold of

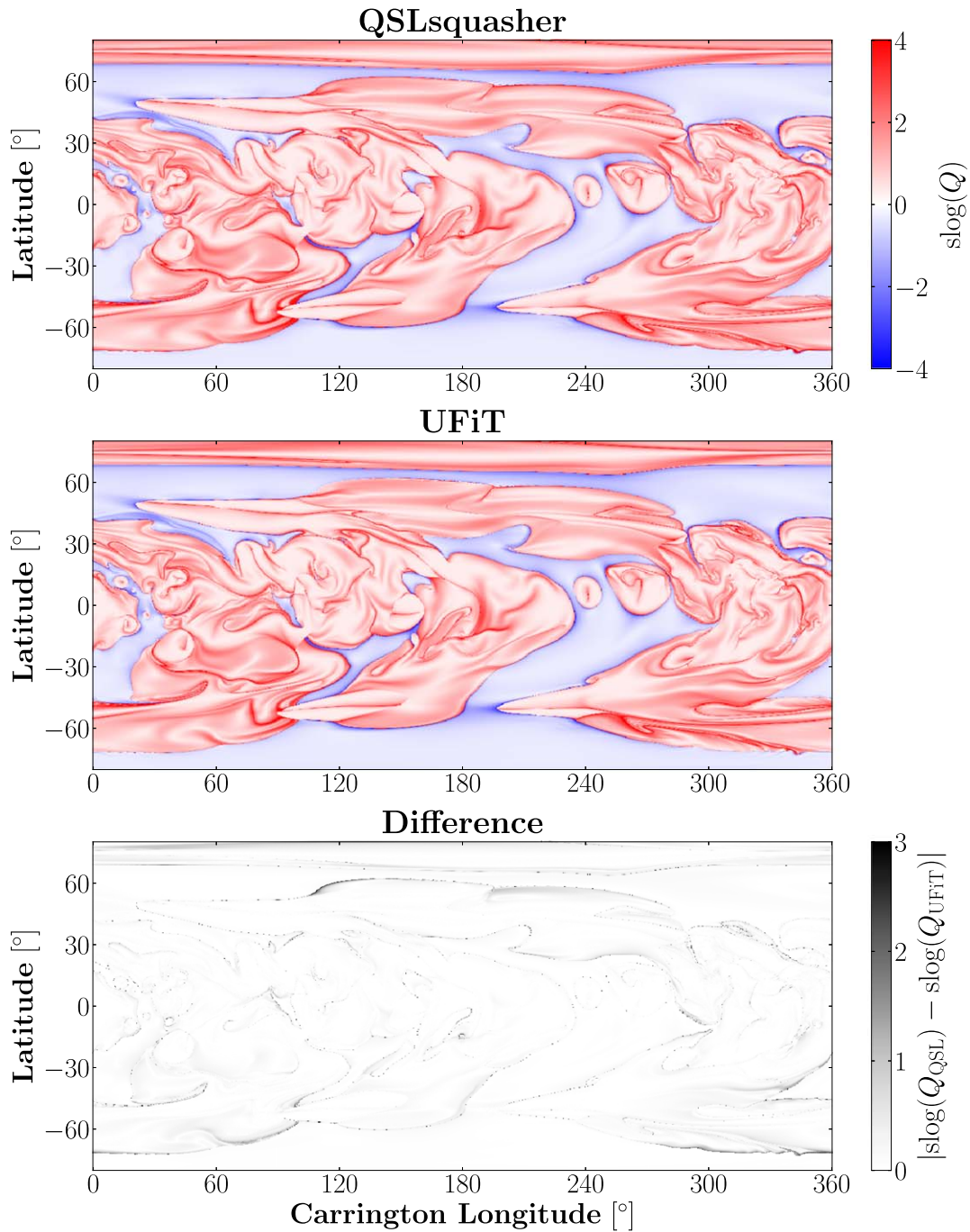


Figure 3. Comparison of the signed logarithm of the squashing factor computed by `QSLsquasher` (upper) and `UFiT` (middle) at $r = R_\odot$ in a magnetofrictional simulation of the corona on 1992 February 4. The absolute difference between the two codes (lower) shows narrow features along separatrices, such as the open-closed boundary, but otherwise close agreement.

0.5. Marching cubes is a generic algorithm for creating an isosurface of some constant value from a three-dimensional scalar field. A similar approach is used for the FDFS, except the label of 0 is applied to the seed points of disconnected field lines and 1 otherwise.

The flux surface of d_{CHB} is straightforwardly calculated with `UFiT` as follows:

1. The field line end points at each point in the three-dimensional volume are saved.
2. Open, closed, and disconnected field lines are identified.
3. For open field lines, identify the footprint.
4. For closed field lines, calculate the minimum distance from (θ, ϕ) of each of the footpoints to the nearest coronal hole boundary; for open field lines, do this for the singular footpoint and set this to a negative number; for disconnected field lines, set this to $\sim -r_{\text{max}}$ or some similarly large negative number.
5. Use the above marching cubes algorithm to calculate an isosurface with d_{CHB} (positive or negative as required) as the threshold value.

This procedure can be repeated for any relevant method of labeling every point in three dimensions based on its local

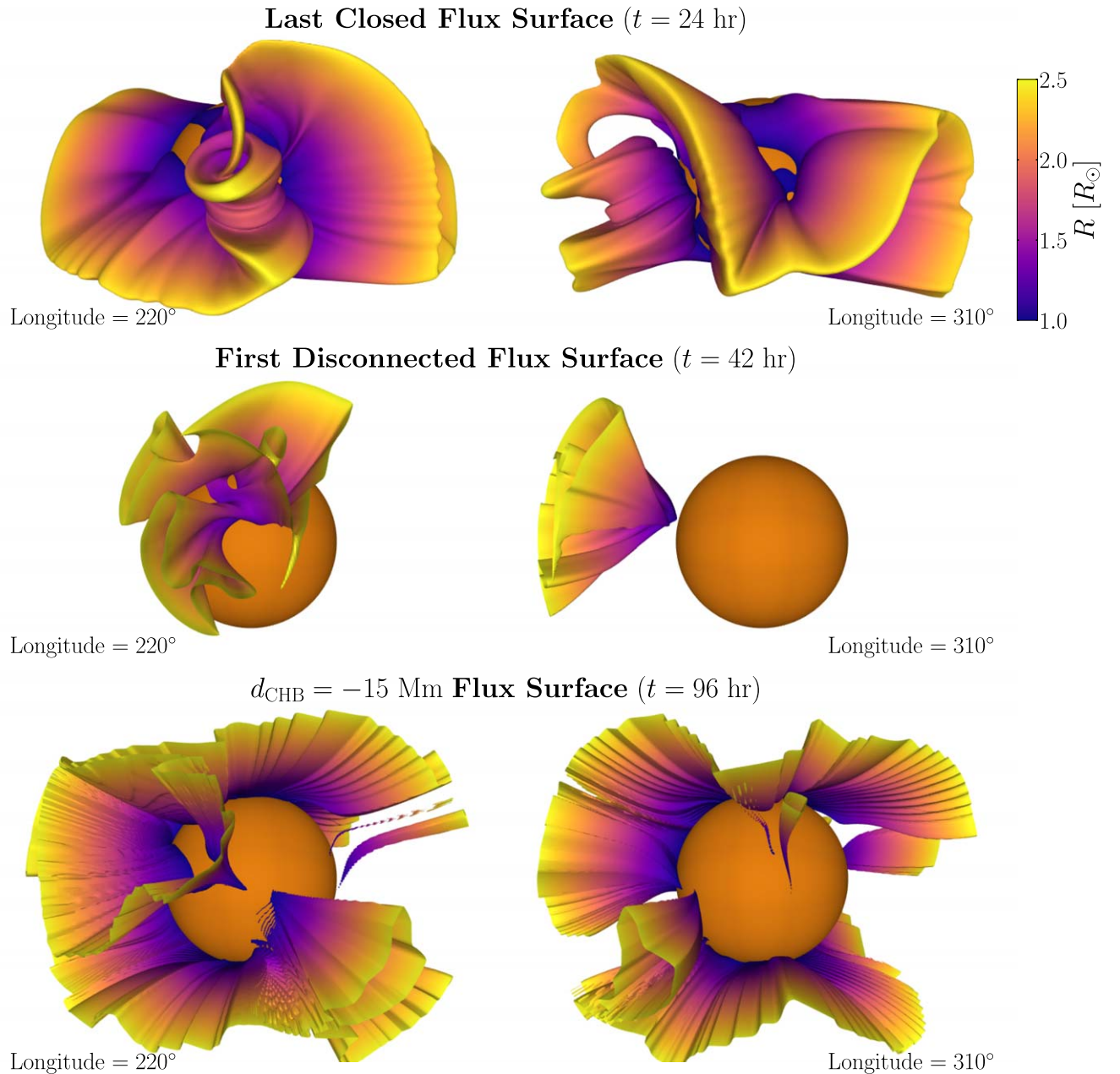


Figure 4. Flux surfaces at various times during an eruption, simulated in DUMFRIC. (upper) LCFS 24 hr after the emergence of Active Region 12672, showing knotted structures during magnetic reconnection. (Middle) FDFS 42 hr after the emergence of the active region. (Lower) Flux surface corresponding to a signed coronal hole boundary distance $d_{\text{CHB}} = -15$ Mm (the negative sign denoting open field lines), meaning that on one side of this surface are all the open field lines with a footpoint further than 15 Mm from a coronal boundary, 96 hr after the emergence of the active region. The active region is at a Carrington longitude of 220° . The images are viewed from above the equator, either directly above the active region, or 90° to the side as indicated. The animated version of this figure involves a view angle rotating in ϕ , showing these surfaces from all directions.

(An animation of this figure is available in the [online article](#).)

properties, or some function of its mapping to the grid boundaries.

A rapid calculation of field line mappings allows volumetric quantities of interest to be evaluated. For example, for the field configuration in Figure 4(c), we find that 81.4% of the coronal volume consists of open field lines. Moreover, we can determine the volume inside an arbitrary flux surface described above. In other words, this is the volume where open field lines have d_{CHB} below some threshold value. The variation of the fraction of the open corona with footpoints falling outside a given distance from a coronal hole boundary is shown in

Figure 5. This type of analysis may allow the true width of coronal holes to be estimated.

Another application of volumetric squashing factor calculations is to make images of the synthetic emission from the corona, to be compared with observations. This can be done by assigning an intensity using the method of Mikić et al. (2018),

$$I \propto \int_{\text{LOS}} \exp(-r) \log_{10} |Q| ds, \quad (33)$$

where s is the line-of-sight coordinate from a given point. A more complicated method involving Gaussian weighting could

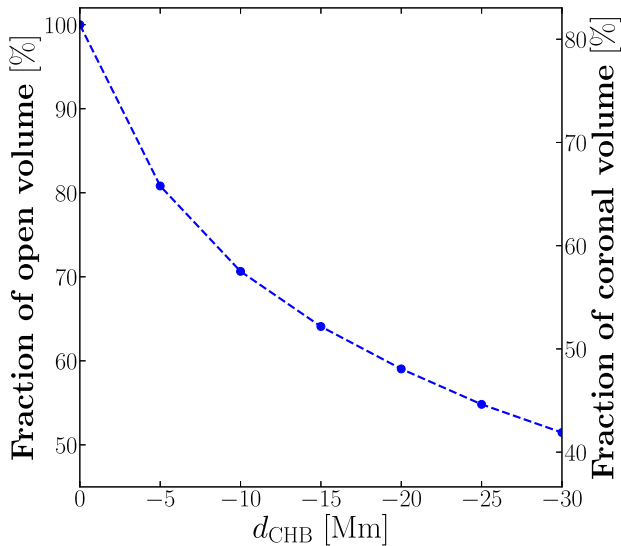


Figure 5. Fraction of coronal volume in which field lines map to the photosphere with signed coronal hole distance d_{CHB} below the values indicated. Note that the negative sign of d_{CHB} corresponds to open field lines, so the more negative distances correspond to the centers of coronal holes.

also be used. Figure 6 shows two examples of synthetic coronagraphs produced by UFiT using this method. The upper example is of the corona during solar maximum at 12:00 on 1992 February 4 (the situation depicted in Figure 3), while the lower example is during solar minimum at 12:00 on 2017 August 25 with a viewpoint of 220° Carrington longitude (the situation on the lower left of Figure 4). The magnetic field in both cases was taken from the long-term magnetofrictional simulation outlined above. These images have a clear similarity with coronal observations and can be computed within minutes even on a common laptop computer.

5. S-Web Evolution

The rapid calculation of field line connectivities and the squashing factor in a three-dimensional grid allows the complexity of the coronal magnetic field and the temporal evolution of the S-Web to be quantified. We have postprocessed a long-term magnetofrictional simulation by using UFiT to compute Q on a grid of (120, 480, 960) points in (r, θ, ϕ) (including the curvature terms). Results were obtained at weekly intervals for the year 1981—a strong solar maximum of Cycle 21—and 1986—a solar minimum between Cycles 21 and 22. For each week in turn, field lines were traced for two inputs. First, the field was taken by UFiT from the full magnetofrictional simulation. Second, only the photospheric field was taken from the magnetofrictional simulation and supplied as a boundary condition for a PFSS solution to the field using the `pfsspy` package (see Stansby et al. 2020); this was then used as an input to UFiT.

Figure 7 shows slices through the three-dimensional grid at constant values of each of the three coordinates such that the panels are centered on $r = 2.5 R_\odot$, $\theta = 20^\circ$, $\phi = 120^\circ$, at noon on 1981 February 26. This center is chosen as the point on the source surface above an emerging active region. As above, the convention of positive for closed and negative for open field lines is used. Both the magnetofrictional and PFSS models are considered. In the former, swirls of large Q extend upward from the location of the active region. Reconnection across

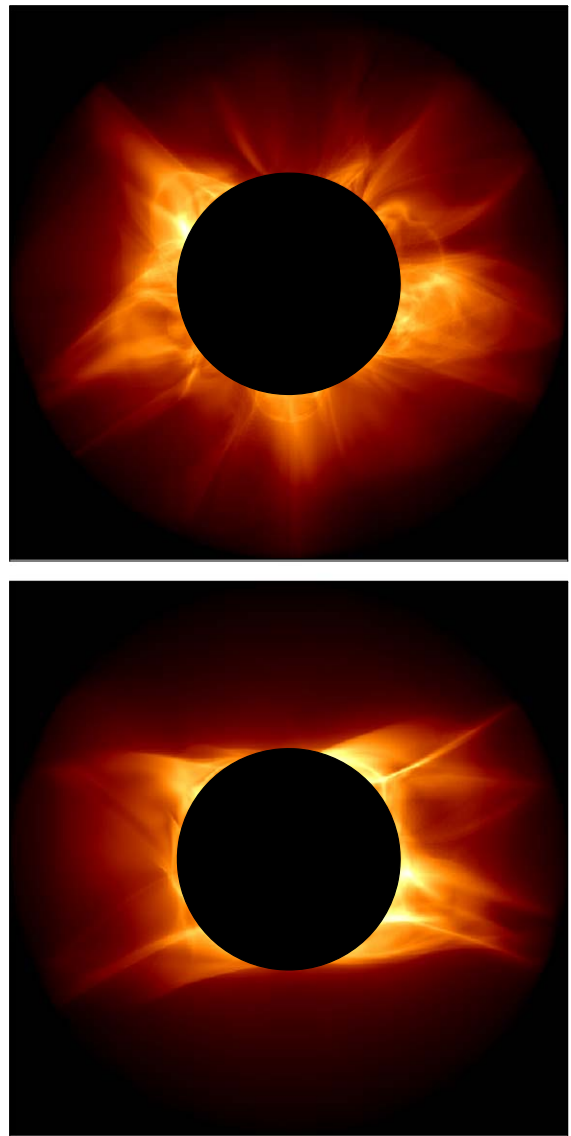


Figure 6. Synthetic coronagraphs computed based on the squashing factor at 12:00 on 1992 February 4, during solar maximum (upper) and at 2017 August 25, during solar minimum (lower).

such separatrices occurs during flares and eruptions. The magnetic field in the PFSS model has broadly similar topology, but is notably smooth and placid with regard to fine features. This is expected since potential fields contain no dynamics or current carrying structures, and it has been confirmed by previous studies such as Edwards et al. (2015).

The grid of Q is further postprocessed by the `HQVseg` code (Scott et al. 2018, 2019; Scott 2019). Above a certain threshold, regions are designated as high- Q volumes (HQVs). Analysis of the field topology allows different properties to be assigned to different HQVs. For example, the regions around the helmet streamer belt can be distinguished from all others by the presence of both inward and outward magnetic polarities, as shown at the source surface in respective plots in Figure 7.

The HQVs around the helmet streamers, separate from the helmet streamers and the sum of these two types of region for the time periods mentioned above is shown in Figure 8. The mean and standard deviation are indicated for both magnetofrictional and PFSS models. In the former case, the volumes

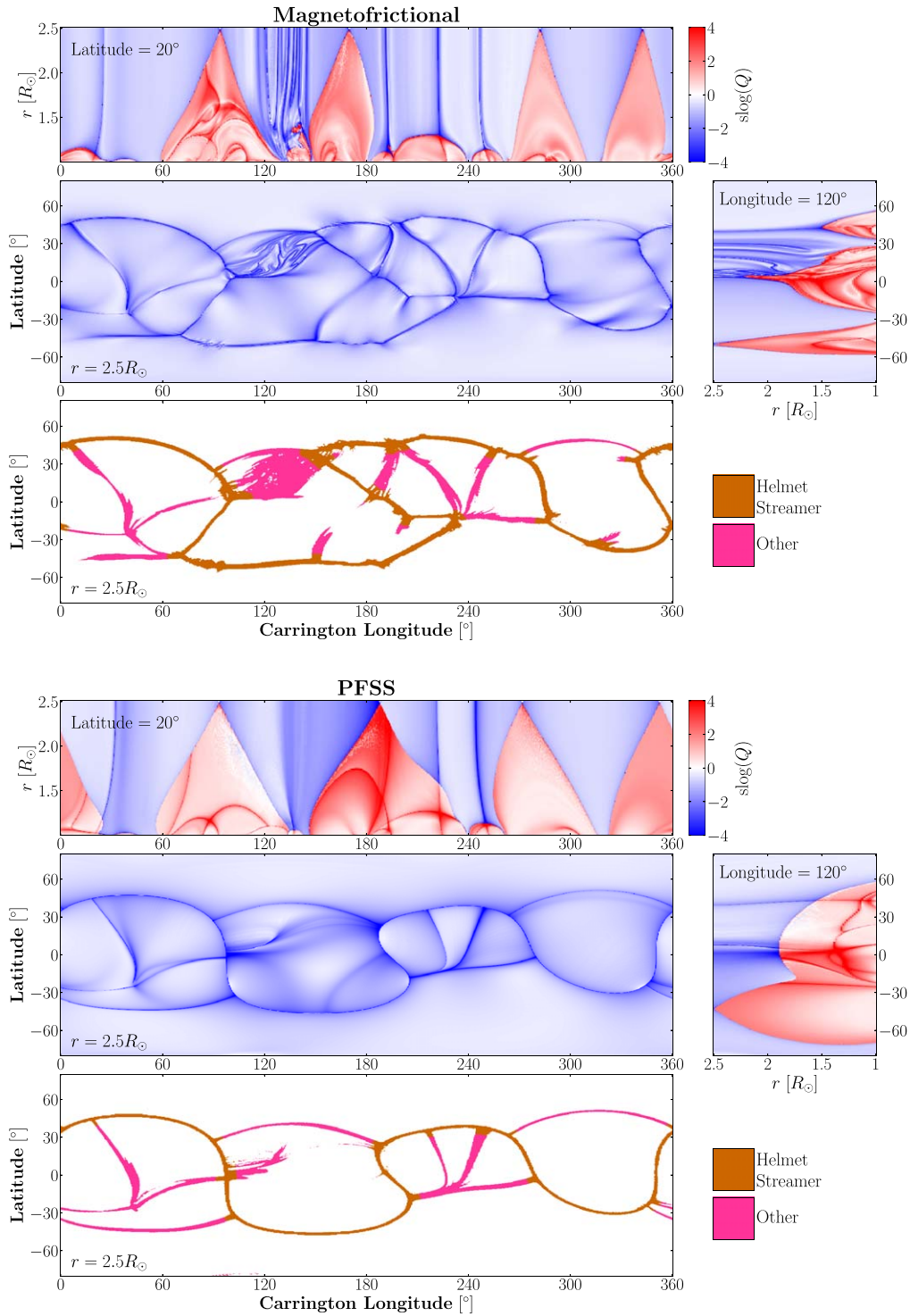


Figure 7. Signed logarithm of the squashing factor Q on 1981 February 26, computed by `UFIT` from the magnetofrictional `DUMFRIC` code (top) and equivalent PFSS solution (bottom). Each slice is at a constant value of r , θ , and ϕ , respectively, as indicated. The lowest panel of each group shows HQVs at the source surface, labeled as belonging to helmet streamers, or otherwise.

during solar maximum clearly exceed solar minimum in both categories and hence also in sum. This straightforwardly agrees with the greater magnetic complexity arising from an increased number of active regions during solar maximum. In the PFSS case, the volumes are uniformly lower than for the magnetofrictional model, and the sum total mean does not differ significantly between solar minimum and maximum, for the reasons outlined above.

6. Conclusion

We have presented a new field line tracing code and associated software libraries for studies of the solar corona. It is intended to be simple to use, requiring commonly used programming languages and libraries. Its main advantage is that it can read the magnetic field directly from a number of commonly used simulation codes, with more added in the

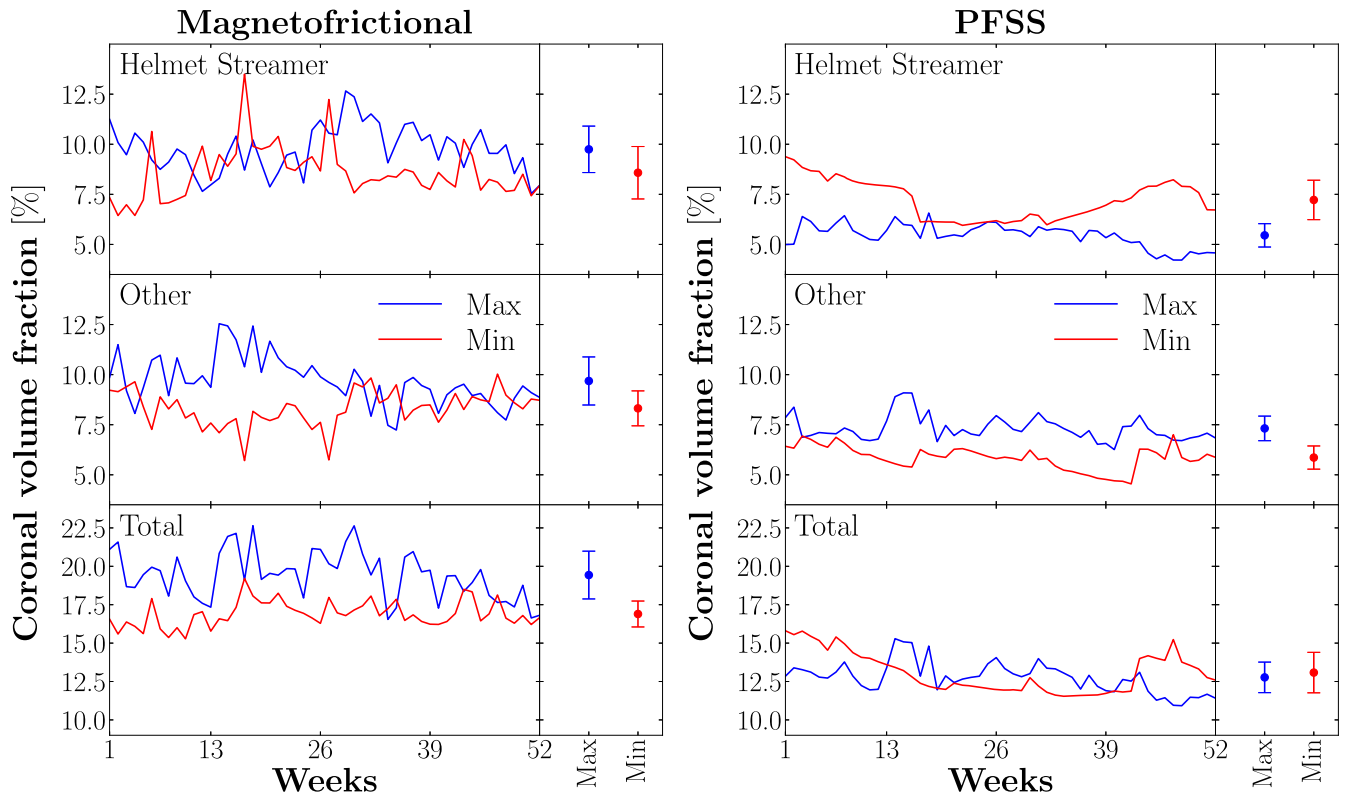


Figure 8. Fraction of the corona occupied by HQVs over the period of a year during solar Maximum (1981, marked “Max”) and Minimum (1986, “Min”). The panels on the left show results for the magnetofrictional `DUMFRIC` code and on the right for the equivalent PFSS solution. The volume is identified as belonging to helmet streamers (top) to other features (middle) and both these groups (bottom). The points on the right of each set of panels show the mean and standard deviation of each respective time series.

future, particularly upon request. The results are returned in a single, self-contained format. When computing the squashing factor Q , we have demonstrated a good degree of numerical accuracy compared to an analytic model and computational performance compared to other codes. We have also demonstrated a number of techniques for visualizing the structure of the corona.

We have used `UFiT` to compute volumetric quantities from a particular snapshot of the corona. For example, we find that 81% of the coronal volume is open; this fraction drops to 60% for open field lines terminating >20 Mm from a given coronal hole boundary. We have also used `UFiT` to generate synthetic images of the corona by integrating a function of the squashing factor along a particular line of sight. Within a longer-term simulation, we have computed the volumes of high Q making up the S-Web, and identified those fractions corresponding to the streamer belt. We find that intuitively the S-Web occupies a larger fraction of corona during solar maximum relative to solar minimum, but only within a more realistic magnetofrictional model, rather than the commonly used PFSS model.

In the future, we intend to extend `UFiT`, which currently uses a first-order integration scheme, to more effective higher-order schemes. One desirable property of such a scheme is reversibility, so that integration forward and backward would return to the original seed point within machine precision; commonly used higher-order integrators like Runge–Kutta do not exhibit this property in general. We next intend to extend our analysis of the dynamic S-Web to cover a continuous magnetofrictional simulation of the previous 4.5 solar cycles. We intend to investigate other methods of dividing up the HQVs, which may elucidate the outflow of the solar wind.

Acknowledgments

The authors would like to thank Jade Touresse for feedback on the `UFiT` code, and acknowledge helpful discussions with Kai Yang regarding K -QSL. This work was supported by UK STFC through grants ST/W001098/1 and ST/W00108X/1. The simulations used resources provided by the Cambridge Service for Data Driven Discovery (CSD3) operated by the University of Cambridge Research Computing Service,⁶ provided by Dell EMC and Intel using Tier-2 funding from the Engineering and Physical Sciences Research Council (capital grant EP/T022159/1), and DiRAC funding from the Science and Technology Facilities Council.⁷ R.B.S. is supported by the Office of Naval Research and by NASA under HSR grant 80HQTR21T0106 and PSP/WISPR grant NNG11EK111.

Appendix A Interpolation

The magnetic field at an arbitrary position inside either regular or adaptive simulation grids is calculated by linear interpolation. A transformation is first made to a cube of unit size, with the original and transformed coordinates defined through

$$x \in [x_0, x_1], \quad (\text{A1})$$

$$\tilde{x} \in [0, 1], \quad (\text{A2})$$

⁶ <https://www.csd3.cam.ac.uk/>

⁷ <https://dirac.ac.uk/>

$$\tilde{x} = \frac{x - x_0}{x_1 - x_0}, \quad (\text{A3})$$

and similarly for the other Cartesian or spherical coordinates as required. Note that the grid is always first transformed from its native one to one of these two coordinate systems (the ARMS and DUMFRIC codes, for example, use $\rho = \log(r)$), before interpolation.

We define a system of coefficients

$$a_1 = f_{100} - f_{000}, \quad (\text{A4})$$

$$a_2 = f_{010} - f_{000}, \quad (\text{A5})$$

$$a_3 = f_{001} - f_{000}, \quad (\text{A6})$$

$$a_4 = f_{110} - f_{100} - f_{010} + f_{000}, \quad (\text{A7})$$

$$a_5 = f_{101} - f_{100} - f_{001} + f_{000}, \quad (\text{A8})$$

$$a_6 = f_{011} - f_{010} - f_{001} + f_{000}, \quad (\text{A9})$$

$$a_7 = f_{111} - f_{110} - f_{101} - f_{011} + f_{100} + f_{010} + f_{001} - f_{000}, \quad (\text{A10})$$

where the value of the original function at the eight cube vertices is denoted by $f_{000} \equiv f(\tilde{x} = 0, \tilde{y} = 0, \tilde{z} = 0)$, $f_{100} \equiv f(\tilde{x} = 1, \tilde{y} = 0, \tilde{z} = 0)$, and so on.

The interpolant function is given by

$$f(\tilde{x}, \tilde{y}, \tilde{z}) = f_{000} + a_1\tilde{x} + a_2\tilde{y} + a_3\tilde{z} + a_4\tilde{x}\tilde{y} + a_5\tilde{x}\tilde{z} + a_6\tilde{y}\tilde{z} + a_7\tilde{x}\tilde{y}\tilde{z}. \quad (\text{A11})$$

Derivatives of the interpolated quantities are computed by differentiating Equation (A11) directly, leading to the algebraic expression

$$\frac{\partial f}{\partial x} = \frac{\partial f}{\partial \tilde{x}} \frac{\partial \tilde{x}}{\partial x} \quad (\text{A12})$$

$$= \frac{1}{x_1 - x_0} (a_1 + a_4\tilde{y} + a_5\tilde{z} + a_7\tilde{y}\tilde{z}) \quad (\text{A13})$$

and similarly for the other coordinates. This method is advantageous due to its computational simplicity when the a coefficients are already calculated as part of the interpolation routine. The problem with linear interpolation is that it produces constant derivatives, which leads to a *checkerboard* pattern when computing Q . This effect can be mitigated by normalizing \mathbf{B} for the purposes of field line tracing and vector transport.

Appendix B Field Lines and Lie Transport

The equation for the parameterized position $\mathbf{X}(s)$ along a field line is given by

$$\frac{d}{ds}\mathbf{X}(s) \equiv (\mathbf{B} \cdot \nabla)\mathbf{X}(s) = \mathbf{B}, \quad (\text{B1})$$

while the Lie transport equation for a vector $\mathbf{U}(s)$ that transforms under the push-forward along $\mathbf{X}(s)$ is given by

$$\frac{d}{ds}\mathbf{U}(s) \equiv (\mathbf{B} \cdot \nabla)\mathbf{U}(s) = (\mathbf{U}(s) \cdot \nabla)\mathbf{B}. \quad (\text{B2})$$

Here \mathbf{B} is understood to be a function of $\mathbf{X}(s)$ and ∇ is the gradient operator. In component form $\mathbf{B} = B_i\hat{e}_i$ for some set of orthonormal basis vectors \hat{e}_i , and similarly for the components

of $\mathbf{U} = U_i\hat{e}_i$, with the usual implied summation over repeated indices.

The directional derivative (of a test function \circ) along \mathbf{B} is then given in terms of the components of \mathbf{B} as

$$\mathbf{B} \cdot \nabla(\circ) \equiv B_i\hat{e}_i \cdot \hat{e}_j \frac{\partial}{\partial q_j}(\circ) = B_i \frac{\partial}{\partial q_i}(\circ), \quad (\text{B3})$$

and similarly for the directional derivative along \mathbf{U} . The weighted partial derivatives $\partial/\partial q_i \equiv g_{ij}^{-1/2} \partial/\partial x_j$ implicitly account for the coordinate metric g_{ij} , which is the identity in Cartesian coordinates, while for spherical coordinates g_{ij} has (only) diagonal elements $\{1, r^2, r^2 \sin^2 \theta\}$. Equation (B1) implicitly defines the affine parameter s so that

$$\frac{d}{ds}(\circ) \equiv B_i \frac{\partial}{\partial q_i}(\circ), \quad (\text{B4})$$

while the physical distance, l , along the field line is given implicitly through

$$\frac{d}{ds}(\circ) \equiv |\mathbf{B}| \frac{d}{dl}(\circ). \quad (\text{B5})$$

In order to solve Equations (B1) and (B2) (from suitable initial conditions) we must rewrite them as a set of ordinary differential equations in s (or l) for each component of \mathbf{X} and \mathbf{U} . In Cartesian (cart) coordinates this is straightforward since only the components of \mathbf{X} and \mathbf{U} change along s . The field line Equation (B1) then becomes

$$\begin{aligned} \frac{d}{ds}\mathbf{X}^{(\text{cart})}(s) &= \hat{x} \frac{d}{ds}x(s) + \hat{y} \frac{d}{ds}y(s) + \hat{z} \frac{d}{ds}z(s) \\ &= \hat{x}B_x + \hat{y}B_y + \hat{z}B_z, \end{aligned} \quad (\text{B6})$$

while the Lie transport equation is

$$\begin{aligned} \frac{d}{ds}\mathbf{U}^{(\text{cart})}(s) &= \hat{x} \frac{d}{ds}U_x(s) + \hat{y} \frac{d}{ds}U_y(s) + \hat{z} \frac{d}{ds}U_z(s) \\ &= \hat{x}B_i \frac{\partial}{\partial x_i}B_x + \hat{y}B_i \frac{\partial}{\partial x_i}B_y + \hat{z}B_i \frac{\partial}{\partial x_i}B_z. \end{aligned} \quad (\text{B7})$$

The component equations for the evolution of $\mathbf{X}(s)$ and $\mathbf{U}(s)$ in Cartesian are, therefore,

$$\frac{d}{ds}x(s) = B_x, \quad (\text{B8})$$

$$\frac{d}{ds}y(s) = B_y, \quad (\text{B9})$$

$$\frac{d}{ds}z(s) = B_z, \quad (\text{B10})$$

and

$$\frac{d}{ds}U_x(s) = \left(U_x \frac{\partial}{\partial x} + U_y \frac{\partial}{\partial y} + U_z \frac{\partial}{\partial z} \right) B_x, \quad (\text{B11})$$

$$\frac{d}{ds}U_y(s) = \left(U_x \frac{\partial}{\partial x} + U_y \frac{\partial}{\partial y} + U_z \frac{\partial}{\partial z} \right) B_y, \quad (\text{B12})$$

$$\frac{d}{ds}U_z(s) = \left(U_x \frac{\partial}{\partial x} + U_y \frac{\partial}{\partial y} + U_z \frac{\partial}{\partial z} \right) B_z. \quad (\text{B13})$$

In spherical (sph) coordinates the basis elements \hat{e}_i are not constant, and the variation in \mathbf{e}_i along $\mathbf{X}(s)$ must be accounted for. Here, we proceed with the convention that $\{r, \theta, \phi\}$ define

a right-handed coordinate system with θ increasing away from the north pole and $\hat{\mathbf{e}}_r \times \hat{\mathbf{e}}_\theta = \hat{\mathbf{e}}_\phi$. In terms of these coordinates, the matrix of partial derivatives $\partial \hat{\mathbf{e}}_i / \partial x_j$ is given by

$$\begin{array}{c|ccc} & \hat{\mathbf{e}}_r & \hat{\mathbf{e}}_\theta & \hat{\mathbf{e}}_\phi \\ \hline \partial_r & 0 & 0 & 0 \\ \partial_\theta & +\hat{\mathbf{e}}_\theta & -\hat{\mathbf{e}}_r & 0 \\ \partial_\phi & +\sin\theta \hat{\mathbf{e}}_\phi & +\cos\theta \hat{\mathbf{e}}_\phi & -(\sin\theta \hat{\mathbf{e}}_r + \cos\theta \hat{\mathbf{e}}_\theta) \end{array} \quad (\text{B14})$$

with each entry corresponding to the resultant found when differentiating the basis vector from the associated column with respect to the coordinate from the associated row.

Noting that the position vector in spherical coordinates is $\mathbf{X}^{(\text{sph})}(s) = r(s)\hat{\mathbf{e}}_r$, we can write (B1) as

$$\frac{d}{ds}\mathbf{X}^{(\text{sph})}(s) = \hat{\mathbf{e}}_r \frac{d}{ds}r(s) + r(s) \frac{d}{ds}\hat{\mathbf{e}}_r = B_r \hat{\mathbf{e}}_r + B_\theta \hat{\mathbf{e}}_\theta + B_\phi \hat{\mathbf{e}}_\phi. \quad (\text{B15})$$

The variation in $\hat{\mathbf{e}}_r$ along s can then be written as

$$\frac{d}{ds}\hat{\mathbf{e}}_r = \left(\frac{\partial}{\partial r}\hat{\mathbf{e}}_r\right) \frac{d}{ds}r(s) + \left(\frac{\partial}{\partial \theta}\hat{\mathbf{e}}_r\right) \frac{d}{ds}\theta(s) + \left(\frac{\partial}{\partial \phi}\hat{\mathbf{e}}_r\right) \frac{d}{ds}\phi(s), \quad (\text{B16})$$

from which it follows that

$$\begin{aligned} \hat{\mathbf{e}}_r \frac{d}{ds}r(s) + \hat{\mathbf{e}}_\theta r \frac{d}{ds}\theta(s) + \hat{\mathbf{e}}_\phi r \sin\theta \frac{d}{ds}\phi(s) \\ = B_r \hat{\mathbf{e}}_r + B_\theta \hat{\mathbf{e}}_\theta + B_\phi \hat{\mathbf{e}}_\phi. \end{aligned} \quad (\text{B17})$$

The individual components of the field line Equation (B1) in spherical coordinates are therefore given by

$$\frac{d}{ds}r(s) = B_r, \quad (\text{B18})$$

$$\frac{d}{ds}\theta(s) = \frac{1}{r}B_\theta, \quad (\text{B19})$$

$$\frac{d}{ds}\phi(s) = \frac{1}{r \sin\theta}B_\phi. \quad (\text{B20})$$

We similarly expand the Lie transport Equation (B2) into components as

$$\frac{d}{ds}\mathbf{U}^{(\text{sph})}(s) = \hat{\mathbf{e}}_i \frac{d}{ds}U_i + U_i \frac{d}{ds}\hat{\mathbf{e}}_i = \hat{\mathbf{e}}_j U_i \frac{\partial}{\partial q_i} B_j + B_j U_i \frac{\partial}{\partial q_i} \hat{\mathbf{e}}_j. \quad (\text{B21})$$

Then, making use of Equation (B4) and exchanging repeated indices, we have

$$\hat{\mathbf{e}}_i \frac{d}{ds}U_i = \hat{\mathbf{e}}_i U_j \frac{\partial}{\partial q_j} B_i + B_i U_j \frac{\partial}{\partial q_j} \hat{\mathbf{e}}_i - U_i B_j \frac{\partial}{\partial q_j} \hat{\mathbf{e}}_i, \quad (\text{B22})$$

where the terms on the right-hand side (RHS) of Equation (B22) can be computed directly from the spatial variation in \mathbf{B} and the local value of the components of \mathbf{U} along $\mathbf{X}(s)$. Finally, after projecting (i.e., left-multiplying) Equation (B22) against individual basis elements \mathbf{e}_k , and exploiting orthonormality ($\hat{\mathbf{e}}_k \cdot \hat{\mathbf{e}}_i = \delta_{ki}$), the k th component of \mathbf{U} satisfies the scalar

ordinary differential equation

$$\frac{d}{ds}U_k = U_j \frac{\partial}{\partial q_j} B_k + (B_i U_j - U_i B_j) \hat{\mathbf{e}}_k \cdot \frac{\partial}{\partial q_j} \hat{\mathbf{e}}_i. \quad (\text{B23})$$

Noting that the last term on the RHS of Equation (B23) is only nonzero for $i \neq j$, the relevant entries for $\partial \hat{\mathbf{e}}_i / \partial x_j$ are

$$\hat{\mathbf{e}}_\theta \cdot \frac{\partial}{\partial \theta} \hat{\mathbf{e}}_r = 1, \quad (\text{B24})$$

$$\hat{\mathbf{e}}_\phi \cdot \frac{\partial}{\partial \phi} \hat{\mathbf{e}}_r = \sin\theta, \quad (\text{B25})$$

$$\hat{\mathbf{e}}_\phi \cdot \frac{\partial}{\partial \phi} \hat{\mathbf{e}}_\theta = \cos\theta. \quad (\text{B26})$$

Substituting these values into Equation (B23) we then have

$$\frac{d}{ds}U_r(s) = U_j \frac{\partial}{\partial q_j} B_r, \quad (\text{B27})$$

$$\frac{d}{ds}U_\theta(s) = U_j \frac{\partial}{\partial q_j} B_\theta + \frac{1}{r} B_r U_\theta, \quad (\text{B28})$$

$$\frac{d}{ds}U_\phi(s) = U_j \frac{\partial}{\partial q_j} B_\phi + \frac{1}{r} B_r U_\phi + \frac{\cos\theta}{r \sin\theta} B_r U_\theta, \quad (\text{B29})$$

where $B_{[i} U_{j]} = (B_i U_j - U_i B_j)$ and

$$U_j \frac{\partial}{\partial q_j} \equiv \left(U_r \frac{\partial}{\partial r} + U_\theta \frac{1}{r} \frac{\partial}{\partial \theta} + U_\phi \frac{1}{r \sin\theta} \frac{\partial}{\partial \phi} \right). \quad (\text{B30})$$

Appendix C Analytic Squashing Factor Derivation

In Section 3 we have validated our methods against the following analytical Q calculation. Consider a potential field with the boundary condition $B_r(R_\odot, \theta, \phi) = \cos\theta$. The solution to Laplace's equation in spherical coordinates (subject to Neumann boundary conditions) between the photosphere at $r = R_\odot$ and a source surface at $r = R_{ss}$ (on which $B_\theta = B_\phi = 0$) gives

$$B_r = \frac{R_\odot^3}{r^3} \left(\frac{2R_{ss}^3 + r^3}{R_\odot^3 + 2R_{ss}^3} \right) \cos\theta, \quad (\text{C1})$$

$$B_\theta = \frac{R_\odot^3}{r^3} \left(\frac{R_{ss}^3 - r^3}{R_\odot^3 + 2R_{ss}^3} \right) \sin\theta, \quad (\text{C2})$$

$$B_\phi = 0. \quad (\text{C3})$$

Let us denote the footpoint of an open field line by the point $(R_\odot, \theta_\odot, \phi_\odot)$ and the handhold of the same field line by $(R_{ss}, \theta_{ss}, \phi_{ss})$. The axisymmetry implies that $\phi = \phi_\odot = \phi_{ss}$ all along the field lines. The parameterization of the field line mapping of Equation (B1) in spherical coordinates gives

$$ds = \frac{dr}{B_r} = \frac{rd\theta}{B_\theta}. \quad (\text{C4})$$

Substituting the solutions for B_r , B_θ and integrating gives

$$\int_{R_\odot}^{R_{ss}} \frac{1}{r} \frac{R_{ss}^3 - r^3}{2R_{ss}^3 + r^3} dr = \int_{\theta_\odot}^{\theta_{ss}} \frac{\cos \theta}{\sin \theta} d\theta, \quad (\text{C5})$$

which, after some rearranging, gives

$$\sqrt{\frac{2R_{ss}^3 + R_\odot^3}{3R_\odot R_{ss}^2}} = \frac{\sin(\theta_{ss})}{\sin(\theta_\odot)}. \quad (\text{C6})$$

We will denote the constant on the left-hand side as follows for brevity,

$$C = \sqrt{\frac{2R_{ss}^3 + R_\odot^3}{3R_\odot R_{ss}^2}}. \quad (\text{C7})$$

$$Q(\theta_\odot) = \frac{\sqrt{1 - C^2 \sin^2(\theta_\odot)} \left(1 + \frac{\cos^2(\theta_\odot)}{1 - C^2 \sin^2(\theta_\odot)} \left(1 + \left(\frac{R_{ss}^3 - R_\odot^3}{R_\odot^3 + 2R_{ss}^3} \right)^2 \tan^2(\theta_\odot) \right) \right)}{\sqrt{\cos^2(\theta_\odot) + \left(\frac{R_{ss}^3 - R_\odot^3}{R_\odot^3 + 2R_{ss}^3} \right)^2 \sin^2(\theta_\odot)}}. \quad (\text{C16})$$

This implies that the separatrices have footpoints at

$$\theta_{\text{QSL}} = \lim_{\theta_{ss} \rightarrow \pi/2} \theta_\odot = \arcsin(1/C). \quad (\text{C8})$$

Using Equations (C6) and (C7) we can define the mapping of the open magnetic field lines for $R_\odot \leq r \leq R_{ss}$ in terms of the function

$$\Theta(\theta_\odot, \phi_\odot) = \theta_{ss} = \arcsin(C \sin(\theta_\odot)). \quad (\text{C9})$$

This allows the norm N in Equation (28) to be calculated in spherical coordinates (using Titov 2007, Equation (38)) as

$$N^2 = \text{Tr}(D^T G^* D G), \quad (\text{C10})$$

where

$$D = \begin{pmatrix} 1 & 0 \\ 0 & \frac{C \cos(\theta_\odot)}{\sqrt{1 - C^2 \sin^2(\theta_\odot)}} \end{pmatrix} = D^T, \quad (\text{C11})$$

$$G^* = R_{ss}^2 \begin{pmatrix} C^2 \sin^2(\theta_\odot) & 0 \\ 0 & 1 \end{pmatrix}, \quad (\text{C12})$$

and

$$G = \frac{1}{R_\odot^2} \begin{pmatrix} \frac{1}{\sin^2(\theta_\odot)} & 0 \\ 0 & 1 + \left(\frac{R_{ss}^3 - R_\odot^3}{R_\odot^3 + 2R_{ss}^3} \right)^2 \tan^2(\theta_\odot) \end{pmatrix} \quad (\text{C13})$$

(see also Titov 2007, Equations (39) to (41)). We therefore have

$$N^2 = \frac{R_{ss}^2}{R_\odot^2} C^2 \left\{ 1 + \frac{\cos^2(\theta_\odot)}{1 - C^2 \sin^2(\theta_\odot)} \left[1 + \left(\frac{R_{ss}^3 - R_\odot^3}{R_\odot^3 + 2R_{ss}^3} \right)^2 \tan^2(\theta_\odot) \right] \right\}. \quad (\text{C14})$$

The determinant $\det(\mathbf{J})$ is given by the ratio of the normal components of the magnetic field to the flux tube ends,

$$\det(\mathbf{J}) = \frac{\sqrt{\cos^2(\theta_\odot) + \left(\frac{R_{ss}^3 - R_\odot^3}{R_\odot^3 + 2R_{ss}^3} \right)^2 \sin^2(\theta_\odot)}}{\frac{R_\odot^3}{R_{ss}^3} \left(\frac{3R_{ss}^3}{R_\odot^3 + 2R_{ss}^3} \right) \sqrt{1 - C^2 \sin^2(\theta_\odot)}}. \quad (\text{C15})$$

Substituting Equations (C14) and (C15) into Equation (28) gives

Note that this is valid for open field lines with footpoints satisfying $\theta_\odot \leq \theta_{\text{QSL}}$ and $\theta_\odot \geq \pi - \theta_{\text{QSL}}$. For closed field lines with footpoints $\theta_{\text{QSL}} < \theta_\odot < \pi - \theta_{\text{QSL}}$, the mapping is uniform and symmetric about $\theta = \frac{\pi}{2}$. This implies that Q is identically 2 in the closed field region.

ORCID iDs

Valentin Aslanyan  <https://orcid.org/0000-0003-3704-4229>
 Roger B. Scott  <https://orcid.org/0000-0001-8517-4920>
 Chloe P. Wilkins  <https://orcid.org/0000-0002-0154-8380>
 Karen A. Meyer  <https://orcid.org/0000-0001-6046-2811>
 David I. Pontin  <https://orcid.org/0000-0002-1089-9270>
 Anthony R. Yeates  <https://orcid.org/0000-0002-2728-4053>

References

- Abbo, L., Ofman, L., Antiochos, S. K., et al. 2016, *SSRv*, **201**, 55
 Antiochos, S. K., Mikić, Z., Titov, V. S., Lionello, R., & Linker, J. A. 2011, *ApJ*, **731**, 112
 Arge, C. N., Odstrcil, D., Pizzo, V. J., & Mayer, L. R. 2003, in AIP Conf. Proc. 679, SOLAR WIND TEN: Proc. of the Tenth Int. Solar Wind Conf. (Melville, NY: AIP), 190
 Aslanyan, V. 2024, UFIT, GitHub, <https://github.com/Valentin-Aslanyan/UFIT>
 Aslanyan, V., & Meyer, K. A. 2023, UFIT v1.0, Zenodo, doi:10.5281/zenodo.10301324
 Aslanyan, V., Meyer, K. A., Scott, R. B., & Yeates, A. R. 2024, *ApJL*, **961**, 3
 DeVore, C. R. 1991, *JCoPh*, **92**, 142
 Edwards, S. J., Yeates, A. R., Bocquet, F.-X., & Mackay, D. H. 2015, *SoPh*, **290**, 2791
 Kim, T. K., Pogorelov, N. V., Arge, C. N., & Henney, C. J. 2020, *ApJS*, **246**, 40
 Mikić, Z., Downs, C., Linker, J. A., & Caplan, R. M. 2018, *NatAs*, **2**, 913
 Pariat, E., & Démoulin, P. 2012, *A&A*, **541**, A78
 Pesnell, W. D., Thompson, B. J., & Chamberlin, P. C. 2012, *SoPh*, **275**, 3
 Pontin, D. I., & Priest, E. R. 2022, *LRSF*, **19**, 1
 Priest, E. R., & Démoulin, P. 1995, *JGR*, **100**, 443
 Scott, R. B. 2019, HQVseg—A Python Module for Coronal Volume Segmentation, v1.0, Zenodo, doi:10.5281/zenodo.3053417
 Scott, R. B., Pontin, D. I., & Hornig, G. 2017, *ApJ*, **848**, 117

- Scott, R. B., Pontin, D. I., & Wyper, P. F. 2019, *ApJ*, 882, 125
- Scott, R. B., Pontin, D. I., Yeates, A. R., Wyper, P. F., & Higginson, A. K. 2018, *ApJ*, 869, 60
- Stansby, D., Yeates, A., & Badman, S. T. 2020, *JOSS*, 5, 2732
- Tassev, S., & Savcheva, A. 2017, *ApJ*, 840, 89
- Titov, V. S. 2007, *ApJ*, 660, 863
- Titov, V. S., Hornig, G., & Démoulin, P. 2002, *JGRA*, 107, 1164
- Wang, Y.-M., & Sheeley, N. R., J. 1990, *ApJ*, 355, 726
- Yang, K. E. 2024, K-QSL, GitHub, <https://github.com/Kai-E-Yang/QSL>
- Yeates, A. R., & Bhowmik, P. 2022, *ApJ*, 935, 13
- Yeates, A. R., & Hornig, G. 2016, *A&A*, 594, A98
- Zhang, P., Chen, J., Liu, R., & Wang, C. 2022, *ApJ*, 937, 26